

A local stress criterion to assess the effects of hydrogen embrittlement on the fracture strength of notched tensile specimens

Claudio Ruggieri^{a,*}, Diego F.B. Sarzosa^a, Marcelo Paredes^b

^a Department of Naval Architecture and Ocean Engineering, University of São Paulo, São Paulo, Brazil

^b Department of Ocean Engineering, Texas A&M University, TX, USA

ARTICLE INFO

Keywords:

Hydrogen embrittlement
Notched tensile specimens
Finite element analysis
Fracture strength
Stress criterion

ABSTRACT

This work addresses the applicability of a local criterion incorporating the coupling of critical stress and a critical hydrogen concentration to predict hydrogen embrittlement effects on the fracture strength of high strength steels using notched round specimens with different notch root radii. The numerical simulations incorporating a relatively simple hydrogen transport model provide strong support for the adoption of a failure criterion in terms of achieving a critical level of tensile stress coupled to the local hydrogen concentration, which, in turn, enable the construction of a failure locus for the degraded material. For the cases analyzed here, construction of such a failure locus based on a critical combination of maximum principal stress and hydrogen concentration enabled predictions of fracture strength for hydrogen-charged tensile specimens which are in very good agreement with experimental data. Overall, the results presented here lend additional support for further developments of a local stress-based criterion to predict hydrogen embrittlement effects on the fracture strength of high strength steels.

1. Introduction

Accurate assessments of the mechanical integrity and remaining life of high-strength steel alloy components exposed to a hydrogen environment play a key role in the continued and safe operation of critical engineering structures. Hydrogen-induced fracture is of primary interest here as fast diffusion of H atoms through the solid material followed by interaction with crystal defects promotes severe material degradation at several length scales over the micro and macro levels [1]. This complex process, generally termed hydrogen embrittlement (HE), results in marked reduction of ductility and toughness, particularly for various classes of metallic alloys, including high strength steels, which can lead to catastrophic fast fracture of the engineering component at stresses below its design or operational stress. For example, a number of experimental studies have shown that the fracture toughness of degraded material by HE is reduced to as much as 10 ~ 25 % of the fracture toughness value for a hydrogen-free material (see, e.g., Gangloff [2] and Ronevich [3] for illustrative data). Consequently, understanding hydrogen-assisted embrittlement in structural materials and, more specifically, high strength steels is essential to enable safe and reliable operation of critical structural components.

A case of particular interest and major concern involves the potential strong degradation of high strength fasteners for critical marine and

subsea applications. As the oil and gas industry is increasingly expanding its exploration and production activities into deep water offshore locations, several of which are hydrocarbon reservoirs having high pressure and high temperature (HPHT) conditions, the subsea equipment must comply with more stringent requirements and specifications for drilling, completing and producing in more hostile environment. Here, bolted connections and fasteners made of high strength steels, mainly AISI 4140 and 4340 steels, and corrosion resistant alloys, such as UNS N07718 [4] (also commercially known as Inconel 718), remain as the primary joint method of high-integrity subsea systems and are, thus, essential for the long-term performance of the subsea infrastructure. However, in marine environments, these components made of high strength materials are highly susceptible to HE associated with hydrogen generated by corrosion reactions or cathodic protection. While recent studies (see the review articles of Esaklul and Ahmed [5]) have shown that subsea fasteners made of high strength steels, such as AISI 4140 and 4340 alloys, and exposed to cathodic protection can be safely used provided their hardness is limited to ~ 34 HRC [6,7], there are still important discrepancies in several industry standards establishing a hardness threshold criterion not supported by enough data to avoid hydrogen embrittlement [8]. Indeed, ASTM F1941 [9] refers to fasteners having minimum specified hardness above 39 HRC as those susceptible to hydrogen embrittlement, while ISO 898.1 [10]

* Corresponding author.

E-mail address: claudio.ruggieri@usp.br (C. Ruggieri).

<https://doi.org/10.1016/j.tafmec.2023.104045>

Received 13 May 2023; Received in revised form 3 August 2023; Accepted 5 August 2023

Available online 18 August 2023

0167-8442/© 2023 Elsevier Ltd. All rights reserved.

indicates that fasteners of class 12.9 with tensile strength of 1200 MPa and having a hardness in the range of 39 ~ 44 HRC are those susceptible to stress corrosion cracking. Fitness-for-service analyses of in-service components under hydrogen embrittlement conditions should employ failure criteria incorporating a more physically-based description of HE micromechanism and which allow relatively simple and conservative assessments most appropriate for engineering-level applications. Perhaps more importantly, with the increased use of high-strength materials to meet the more stringent demands of HPHT conditions often present in challenging deep-water oil and gas reservoirs [11], development of more effective and realistic approaches addressing the effects of HE on this class of materials remains essential.

Hydrogen embrittlement is arguably one of the most complex phenomena of degradation in metallic materials, causing a hydrogen-induced transition from a high-toughness ductile fracture (micro-void coalescence) to a brittle-type of fracture (either by a transgranular or intergranular mechanism). While there is now a rapidly growing body of research that focuses on the several mechanisms controlling the effects of HE on the mechanical behavior and, more specifically, on the fracture resistance and toughness of steels and metallic alloys (see, e.g. the review articles of Barrera et al. [1] and Dadfarnia et al. [12]), a consensus appears to be emerging in favor of two most viable mechanisms: (1) *hydrogen induced decohesion* (HID), also known as *hydrogen-enhanced decohesion* (HEDE), in which hydrogen accumulated at locations of high stress triaxiality, such as ahead of a crack tip, reduces the local cohesive strength and the specific surface energy thereby reducing the fracture toughness [13,14] and (2) *hydrogen-enhanced localized plasticity* (HELP), in which hydrogen accumulated in a localized region ahead of a crack tip promotes an increase in dislocation nucleation and mobility thereby increasing plasticity and material softening [15,16]. While it is now recognized that no single mechanism can comprehensively explain all the phenomena associated with HE at the continuum level, several other hydrogen degradation theories have been proposed incorporating different scales and micromechanisms of HE in steels and metallic alloys [1,12] — however, these are not germane to the present study.

In this work, we pursue a line of investigation in which the conditions for intergranular fracture instability associated with hydrogen embrittlement in martensitic high strength steels are accounted for in terms of a local criterion incorporating a coupling of critical stress and a critical hydrogen concentration. To the extent that fracture may be expected controlled by the near-tip stress fields, such a criterion makes contact with a hydrogen-induced decohesion type mechanism that describes macroscopic embrittlement in terms of achieving a critical level of tensile stress over a microstructural length-scale physically coupled to the decrease in local cohesive strength caused by hydrogen diffusion. Recent work by Gonzalez et al. [17] also adopted a similar concept based on a critical distance methodology in connection with a simplified description of the stress fields ahead of a notch to assess effects of hydrogen on the fracture resistance of notched compact tension specimens. Here, we describe the effects of hydrogen-induced degradation on fracture strength by employing a 3-D computational framework incorporating a material constitutive model that extends a conventional Mises plasticity model to include the effect of diffusible hydrogen on the mechanical (flow) properties based on the hydrogen local equilibrium model proposed earlier by Oriani [18]. The experimental investigations conducted by Wang et al. [19–21] provide the quantitative relationship between the tensile strength of notched specimens with varying stress triaxiality and diffusible hydrogen content of a quenched and tempered AISI 4135 steel and a boron-alloyed steel, upon which the influence of hydrogen embrittlement on fracture behavior can be assessed. Those experimental studies demonstrate that the diffusible hydrogen content plays a key role in reducing the fracture strength of the notched specimens with different levels of stress triaxiality. Their studies also show that a criterion based on a critical combination of local stress and local hydrogen concentration was capable of describing the fracture behavior of the hydrogen-charged notched

specimens. Further analyses are also performed on an even higher strength class of martensitic steel tested recently by Nie et al. [22].

The present computational model advances this point of view and enables defining a failure locus that captures accurately the measured variation of fracture strength with hydrogen content fairly independent of specimen stress triaxiality to produce a viable fracture criterion for hydrogen-degraded engineering components. There are important differences between our approach and that of Wang et al. [19–21] in terms of the kinetics of hydrogen diffusion incorporated into the constitutive model and in the way the local stress criterion to assess effects of hydrogen embrittlement is developed. Overall, we believe that there is convincing evidence to support a local stress criterion in terms of a failure locus defining fracture conditions for hydrogen-charged specimens and its potential as an effective tool for assessing the effects of hydrogen embrittlement on the fracture behavior for a large class of structural components.

2. Kinetics of hydrogen diffusion in metals

This section briefly describes an approximate treatment of a hydrogen transport model that has a direct bearing on the computational framework incorporating the effect of diffusible hydrogen on the mechanical (flow) properties addressed later. The approach presented here draws heavily on previous work of Oriani [18] and Sofronis et al. [23, 24], which considers a local equilibrium of diffusible hydrogen in lattice and trapping sites coupled with local stresses and strains. Readers are referred to those studies and the WARP3D [25] documentation for a more complete discussion of the hydrogen transport model under discussion.

2.1. Hydrogen diffusion: Oriani model

Development of a computational model incorporating the effects of hydrogen on the material behavior begins by considering a simplified kinetic model describing the hydrogen diffusion in metals. By assuming that hydrogen resides at either normal interstitial lattice sites (NILS) or at reversible trapping sites, such as microstructural defects generated by plastic deformation [26], and, further, assuming that these two populations are always in equilibrium, Oriani [18] and Oriani e Josephic [27,28] proposed a model to describe the local equilibrium of hydrogen in the traps and lattice in terms of

$$\frac{\theta_T}{1 - \theta_T} = \frac{\theta_L}{1 - \theta_L} \exp\left(\frac{W_B}{RT}\right) \quad (1)$$

where θ_L and θ_T are the occupancies of hydrogen in NILS and trapping sites, W_B represents the trap binding energy, R is the gas constant defined by $8.31 \text{ J mol}^{-1} \text{ K}^{-1}$ and T is the absolute temperature in K. The hydrogen concentration per unit volume in trapping sites, C_T , can be written as

$$C_T = \theta_T \alpha N_T \quad (2)$$

where α defines the number of sites per trap and N_T represents the trap density measured in terms of the number of traps per unit volume, which is a function of the local effective plastic strain. Similarly, the hydrogen concentration residing in NILS is expressed by

$$C_L = \theta_L \beta N_L \quad (3)$$

in which β is the number of NILS per solvent atom and N_L defines the number of solvent atoms per unit lattice volume. If the available number of trapping sites per unit volume, αN_T , is smaller than the available NILS per unit volume, βN_L , then

$$N_L = \frac{N_A}{V_M} \quad (4)$$

where $N_A = 6.0232 \times 10^{23} \text{ atoms/mol}$ is Avogadro's number and V_M defines the molar volume of the host lattice measured in units of volume per lattice mole.

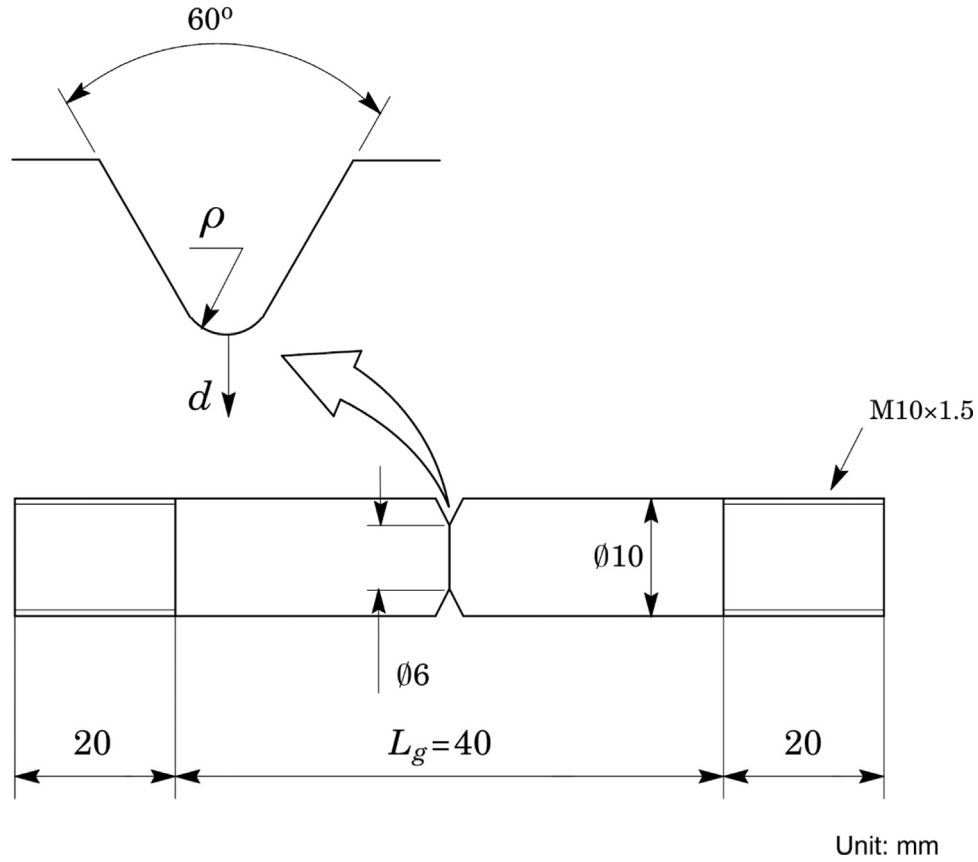


Fig. 1. Geometry of the notched tensile specimen employed in the fracture tests of the hydrogen charged AISI 4135 steels and boron-alloyed steel conducted by Wang et al. [19–21].

2.2. Hydrogen concentration in metals

Further development of a finite element formulation including the effects of hydrogen on the mechanical (flow) properties requires considering the connection between hydrogen transport and the local fields of hydrostatic stress and plastic strain in the material. The hydrogen concentration at NELS, C_L , is assumed to be in equilibrium with local Cauchy stress, σ_{ij} , such that

$$\frac{\theta_L}{1 - \theta_L} = \frac{\theta_L^0}{1 - \theta_L^0} K_L \quad (5)$$

where $\theta_L^0 = C_L^0 / \beta N_L$ is the initial occupancy at NELS and

$$K_L = \exp \left[\frac{\sigma_{kk} V_H}{3RT} \right] \quad (6)$$

is the equilibrium constant determined by the first order interaction between hydrogen-induced lattice dilatation. In the above, the hydrostatic stress is defined as $\sigma_h = \sigma_{kk}/3$ and V_H is the partial molar volume of hydrogen in solution; here, the standard summation convention applies.

Combining Eqs. (4) and (5), and, further, considering that hydrogen trap sites are associated with the effective plastic strain, $\bar{\epsilon}_p$, in the deforming metal, Sofronis et al. [24] arrived at the total hydrogen concentration as

$$C = C_L + C_T = \beta N_L [\theta_L (\sigma_{kk}) + \theta_{TL} (\sigma_{kk}, \bar{\epsilon}_p)] \quad (7)$$

where

$$\theta_L (\sigma_{kk}) = \theta_L^0 K_L / [(1 - \theta_L^0) + \theta_L^0 K_L] \quad (8)$$

and

$$\theta_{TL} (\sigma_{kk}, \bar{\epsilon}_p) = \frac{\alpha N_T (\bar{\epsilon}_p)}{\beta N_L} \times \frac{K_T \theta_L (\sigma_{kk})}{1 - \theta_L (\sigma_{kk}) + K_T \theta_L (\sigma_{kk})} \quad (9)$$

Given that hydrogen remains in equilibrium with local stresses, Eqs. (7)–(9) define the total hydrogen concentration based on current values of $\bar{\epsilon}_p$ and σ_{kk} . Alternatively, the total hydrogen concentration can also be expressed in the unit of hydrogen atoms per host metal atom (H/M) as

$$c = C / N_L = \beta [\theta_L (\sigma_{kk}) + \theta_{TL} (\sigma_{kk}, \bar{\epsilon}_p)] \quad (10)$$

Moreover, since the effective plastic strain and hydrostatic stress also depend on the amount of hydrogen present in the material, it becomes clear that the problem of determining the hydrogen concentration, local stresses and plastic strains requires a fully coupled solution. Readers are referred to the WARP3D [25] documentation for more detailed information about the above formulations.

3. Hydrogen embrittlement of notched tensile specimens

This section presents the necessary results and experimental data measured by Wang et al. [19–21] and also Nie et al. [22] that were employed in the 3-D finite element analyses of hydrogen-charged tensile specimens to quantify the effects of hydrogen on the fracture strength of quenched and tempered, high strength steels addressed in Section 5. Possibly the most notable result derived from those studies is the systematic investigation of the relationship between the levels of stress triaxiality and hydrogen content for different high strength steels under varying conditions, which can be advantageously utilized in the present study. The reader is referred to those works for a full account of the experimental details, including the hydrogen charging procedure.

Wang et al. [19] conducted tensile tests on a hydrogen charged high strength steel using notched round tensile specimens with different notch root radii. The material is a quenched and tempered, low alloy AISI 4135 steel with yield stress, $\sigma_{ys} = 1235$ MPa, and tensile strength, $\sigma_{uts} = 1320$ MPa. Fig. 1 displays the notched round bar specimens employed in

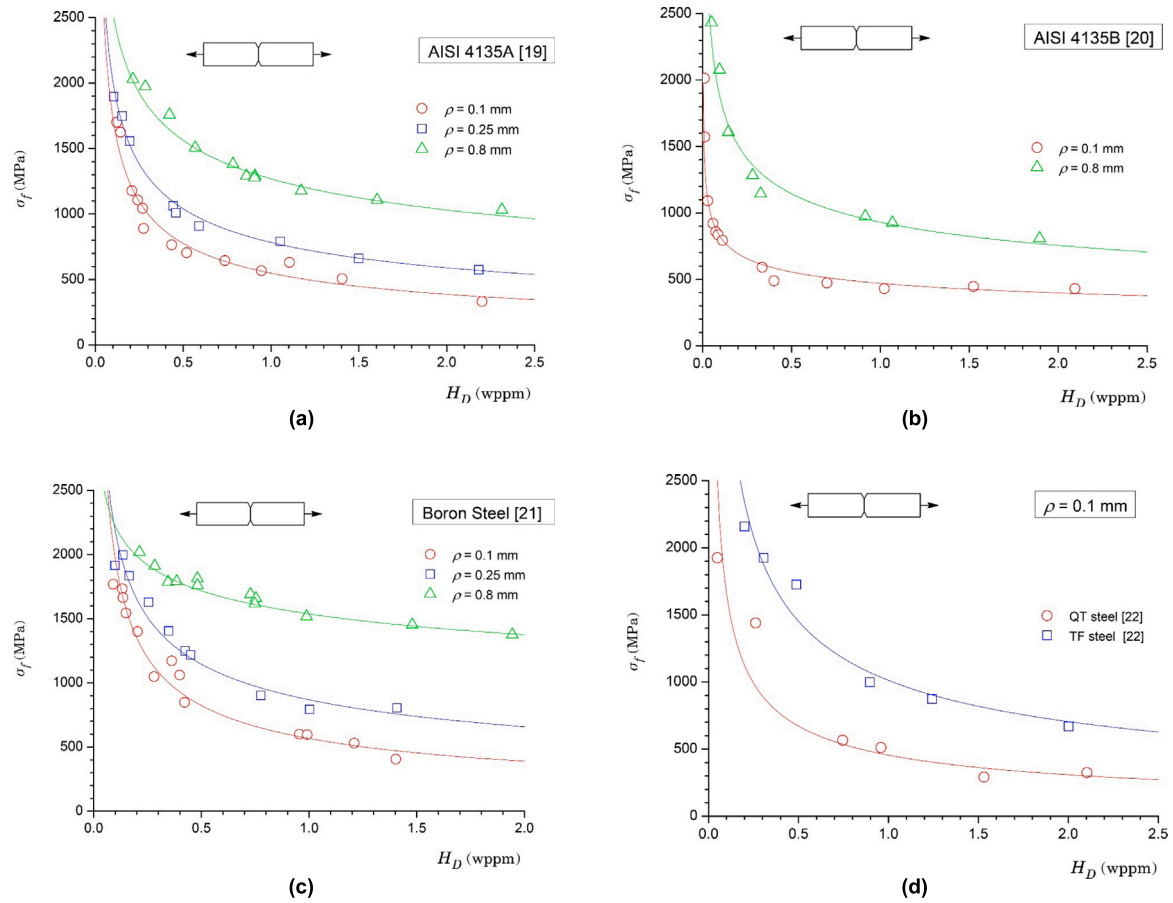


Fig. 2. Dependence of notch tensile strength, σ_f , on diffusible hydrogen content, H_D , for notched round specimens with different notch root radii: (a) Steel 4135 A measured by Wang et al. [19]. (b) Steel 4135B measured by Wang et al. [20]. (c) High strength boron-alloyed steel measured by Wang et al. [21]. (d) TF and QT steels measured by Nie et al. [22].

their tensile tests, in which the notch radius, ρ , is 0.1, 0.25 and 0.8 mm, and the gage length, L_g , is 40 mm. Hydrogen charging of the tensile specimens was performed by an electrochemical method using either an acidic or alkaline aqueous solution at various current densities. Following hydrogen charging of the steel, slow strain rate tensile (SSRT) tests were carried out to determine the dependence of notch tensile strength on diffusible hydrogen content for the notched specimens. In later related work, Wang et al. [20] also performed tensile tests on a hydrogen charged AISI 4135 steel having a different quenching and tempering treatment and with yield stress, $\sigma_{ys} = 1320$ MPa, and tensile strength, $\sigma_{uts} = 1450$ MPa. Here, SSRT tests were also conducted to evaluate the effect of diffusible hydrogen content on the tensile strength for notched specimens with $\rho = 0.1$ and 0.8 mm — these specimens have the same configuration as those already shown in Fig. 1. In the interest of clarity, these materials are hereafter simply referred to as 4135 A ($\sigma_{ys} = 1235$ MPa) and 4135B ($\sigma_{ys} = 1320$ MPa). Additional tensile tests using notched round specimens were also performed by Wang et al. [21] on a quenched and tempered, boron-alloyed steel with yield stress, $\sigma_{ys} = 1160$ MPa, and tensile strength, $\sigma_{uts} = 1305$ MPa. The specimen configuration, hydrogen charging procedure and SSRT tests are essentially similar to those already described previously for the testing program conducted on the AISI 4135 steel. For convenience, Table 1 summarizes the mechanical properties under discussion and also includes the strain hardening exponent, n , appearing in Eq. (11) presented later. Here, parameter n is readily estimated from API 579 [29] using the yield stress and tensile strength values.

Figs. 2(a–c) show the dependence of experimental fracture stress, σ_f , on diffusible hydrogen content, H_D , for the notched round specimens with different notch root radii measured by Wang et al. [19–21]

Table 1

Mechanical properties in terms of yield stress, σ_{ys} , and tensile strength, σ_{uts} , for all the tested material, including the strain hardening exponent, n , derived from API 579 [29].

Material	σ_{ys} (MPa)	σ_{uts} (MPa)	n
Steel 4135A	1235	1320	28
Steel 4135B	1320	1450	22
Boron Steel	1160	1305	19
QT Steel	1380	1580	18
TF Steel	1460	1540	32

for steels 4135 A and 4135B, and the boron-alloyed steel. In these plots, the fracture stress is defined as $\sigma_f = F_{max}/A_{0-net}$, in which F_{max} represents the maximum tensile load attained in the tests and A_{0-net} is the initial cross-section net area of the notch. Further, Wang et al. [19–21] also conducted a power law fitting of the experimental results, as indicated by the lines displayed in the figures, in the form $\sigma_f = kH_D^m$, where k and m are constants. Table 2 provides parameters k and m reported by Wang et al. [19–21] for each set of experimental data. Observe that the fracture stress decreases rather dramatically, particularly for the notched specimens with smaller radius, ρ , with only a small amount of hydrogen content. For example, in the case of steel 4135 A and $\rho = 0.1$ mm, the fracture stress decreases from $\sigma_f \approx 1800$ MPa at $H_D \approx 0.1$ wppm to $\sigma_f \approx 1000$ MPa at $H_D \approx 0.3$ wppm, as indicated in Fig. 2(a). The variation of σ_f with H_D for steel 4135 B and $\rho = 0.1$ mm is even more severe, as can be seen in Fig. 2(b). Essentially similar trends are also observed for the results of the boron-alloyed steel shown in Fig. 2(c).

In another related work to characterize effects of hydrogen embrittlement on high strength structural steels, Nie et al. [22] conducted

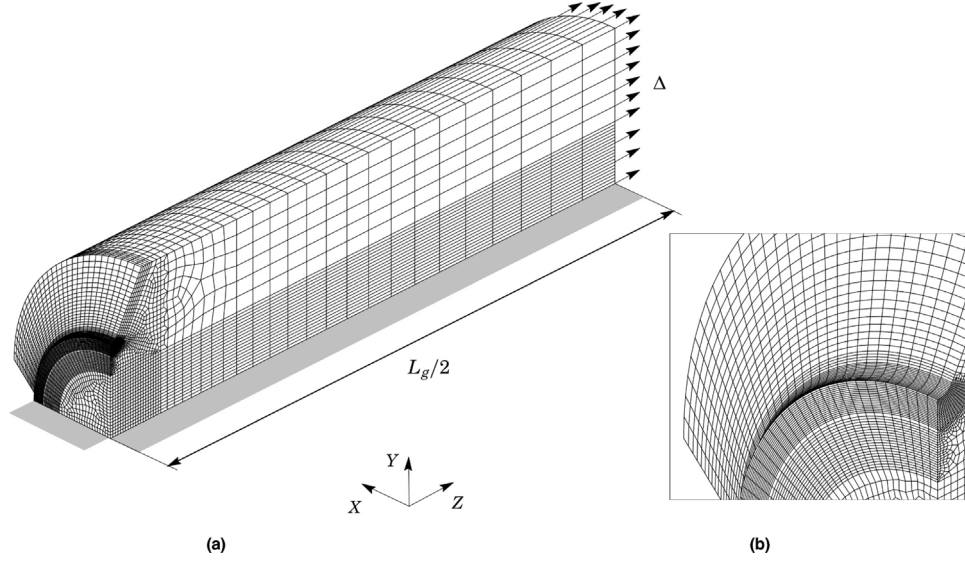


Fig. 3. (a) 3-D finite element mesh for the notch round tensile specimens with a root radius of $\rho = 0.25$ mm. (b) Meshing detail of the notch root region.

Table 2

Parameters k and m describing the power law fitting of experimental fracture stress versus hydrogen concentration for the tested high strength steels [19–22].

Material	ρ (mm)	k	m
Steel 4135A	0.1	548	−0.50
	0.25	783	−0.41
	0.8	1269	−0.30
Steel 4135B	0.1	470	−0.24
	0.8	930	−0.30
Boron Steel	0.1	566	−0.54
	0.25	868	−0.40
	0.8	1537	−0.16
QT Steel	0.1	455	−0.56
TF Steel	0.1	1012	−0.52

SSRT tests on a hydrogen charged, ultrahigh tensile strength steel with ultrafine grain structure obtained by two different thermomechanical treatment: (1) an air-cooled steel, denoted as TF sample and (2) a quenched and tempered steel, denoted as QT sample — note that steels B13 and B15 included in Fig. 9 of Nie et al. [22] correspond to the steels 4135 A and 4135B previously described. The fracture tests employ notched round bar specimens with a notch radius, $\rho = 0.1$ mm, which have the same configuration as those employed by Wang et al. [19–21]. The TF material has yield stress, $\sigma_{ys} = 1460$ MPa, and tensile strength, $\sigma_{uts} = 1540$ MPa. Fig. 2(d) provides the variation of experimental fracture stress, σ_f , on diffusible hydrogen content, H_D , for this material and also includes the experimental results for the QT steel having yield stress, $\sigma_{ys} = 1380$ MPa, and tensile strength, $\sigma_{uts} = 1580$ MPa. Table 1 also summarizes the mechanical properties for these materials whereas Table 2 gives parameters k and m for the power law fitting of the experimental results, which, again, follow closely the results already reported in Refs. [19–22]. Here, we observe that, since Nie et al. [22] report only the experimental data set, parameters k and m displayed in the table are obtained by a power law fitting to the experimental values shown in Fig. 2(c). Section 5.5 addresses the potential effects of flow properties on the fracture behavior of hydrogen-charged specimens and compares the failure loci for all the above materials, including the TF and QT steels tested by Nie et al. [22].

4. Computational procedures

4.1. Finite element models

Numerical simulations were performed for detailed 3-D finite element models of the notched tensile specimens previously described to measure the effects of hydrogen embrittlement on fracture strength. The 3-D finite element mesh for the notch round tensile specimen with a root radius of $\rho = 0.25$ mm is displayed in Fig. 3(a–b). The grip conditions are enforced by appropriate constraints in the X and Y directions on nodes located at $Z = L_g/2$. The geometry and loading configuration creates symmetry conditions that permit the use of only one-quarter, 3-D model of the tensile specimens in which displacement controlled loading, as shown in Fig. 3(a), permits extending the numerical computations beyond the maximum load attained in the simulations.

This 3-D finite element model consists of 45,707 nodes 41,716 8-node elements with a more refined mesh describing the notch root region, as displayed in Fig. 3(b). Here, the notch root geometry is modeled by an element size of ≈ 0.02 mm over distances along the net section radius of $\approx 20 \times \rho$ to resolve accurately the stress and strain distribution ahead of the notch. Essentially similar mesh arrangements are used for other 3-D finite element models of the notched tensile specimens having radius $\rho = 0.1$ and 0.8 mm — to conserve space, they are not included here.

4.2. Constitutive model and hydrogen-related parameters

The hydrogen-coupled material model adopted extends a conventional J_2 flow theory with Mises plastic potential to include the effects of solute hydrogen on the flow properties in large geometry change (LGC) setting. Since hydrogen does not affect the macroscopic tensile behavior of unnotched specimens [20], the uniaxial (tensile) stress–strain response for the material can be represented by a power-hardening model in the form

$$\frac{\bar{\epsilon}}{\epsilon_{ys}} = \frac{\bar{\sigma}}{\sigma_{ys}} \quad , \quad \bar{\epsilon} \leq \epsilon_{ys} \quad ; \quad \frac{\bar{\epsilon}}{\epsilon_{ys}} = \left(\frac{\bar{\sigma}}{\sigma_{ys}} \right)^n \quad , \quad \bar{\epsilon} > \epsilon_{ys} \quad (11)$$

where $\bar{\sigma}$ defines the uniaxial true stress, $\bar{\epsilon}$ denotes the logarithmic strain, σ_{ys} and ϵ_{ys} are the reference (yield) stress and strain, and n denotes the strain hardening exponent. The mechanical data given

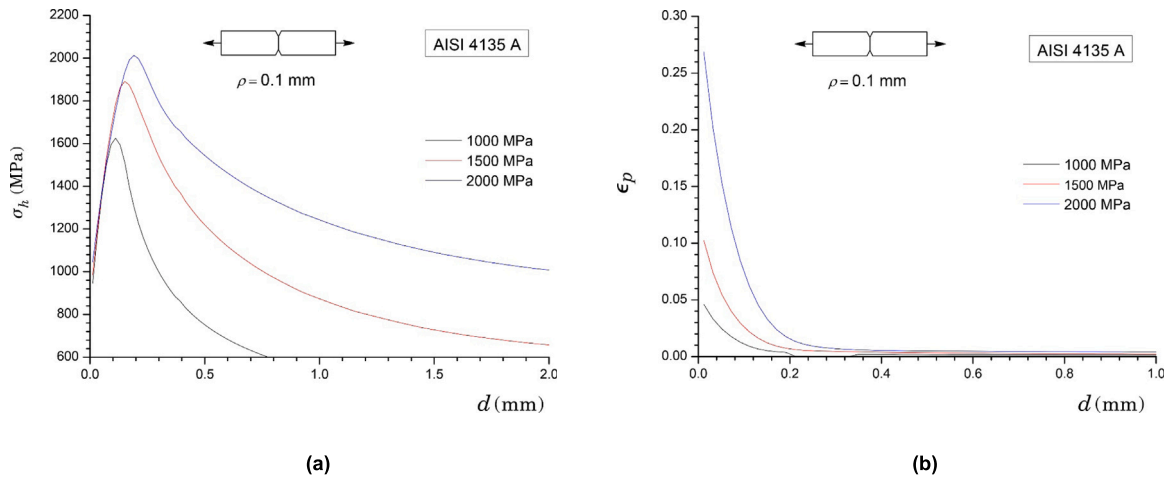


Fig. 4. Computed distributions along the net section for the uncharged specimen with $\rho = 0.1$ mm at three levels of net stress, $\sigma_{net} = 1000, 1500$ and 2000 MPa: (a) hydrostatic stress, σ_h , (b) plastic strain, ϵ_p .

in previous Table 1, including the strain hardening exponent, are employed in the analyses of the materials under discussion. Moreover, the computations also consider the elastic modulus, $E = 206$ GPa and Poisson's ratio, $\nu = 0.3$.

Within the context of finite strain solutions, the Mises yield surface is described in terms of Cauchy (true) stresses, which, in turn, are in equilibrium with hydrogen. The local fields of hydrostatic stress and plastic strain then determine the total hydrogen concentration, as given in previous Eq. (7). The finite element code WARP3D [25] provides the numerical solutions for the 3-D analyses of the notched tensile specimens reported here. Readers are referred to WARP3D user manual for a full account of the constitutive framework and numerical procedures incorporating Mises plasticity in the presence of hydrogen.

To generate the 3-D numerical solutions needed to evaluate the influence of hydrogen on the mechanical behavior for the notched tensile specimens, the hydrogen-model parameters described in Section 2 should be appropriately chosen to reflect the kinetics of hydrogen diffusion for the high strength steels employed in our study. Unfortunately, Wang et al. [19–21] do not provide detailed information on the hydrogen-related parameters for their materials, other than standards values such as the partial molar volume of hydrogen in bcc-Fe. However, reasonably good estimates for the required parameters are obtainable from the work of Novak et al. [30], who reported a study of hydrogen-induced intergranular fracture in a quenched and tempered AISI 4340 steel with 1490 MPa of yield stress. To the extent that those hydrogen-related parameters can be regarded as phenomenological quantities chosen to approximately describe the effects of hydrogen on the flow properties, small parameter variations are compensated by corresponding changes in the content of hydrogen which is in equilibrium with the local fields of hydrostatic stress and plastic strain. Thus, they are not seen of great influence in the fracture strength predictions addressed here. We then proceed to define the following parameters based on the work of Novak et al. [30]: partial molar volume of hydrogen, $V_H = 2.1 \times 10^{-6}$ m³/mol, molar volume of the host metal (Fe), $V_M = 7.11 \times 10^{-6}$ m³/mol, number of sites per trap, $\alpha = 1$, number of NILS per solvent atom, $\beta = 1$, and the trap binding energy, $W = -18$ kJ/mol. This latter parameter is also within the values reported by Ayas et al. [31].

5. Results and discussion

The following sections provide the essential results derived from the 3-D analyses incorporating effects of hydrogen on the fracture strength for the notched tensile specimens discussed previously. The presentation begins with descriptions of variations in key quantities

ahead of the notch in connection with notch radius for uncharged and hydrogen-charged specimens, which have a direct bearing on the mechanical behavior of the specimens. Further, these features are central to establish of a local stress criterion describing effects of hydrogen embrittlement on fracture strength. Then we turn attention to predictions of the notch tensile strength dependence on hydrogen content based on the proposed fracture criterion.

5.1. Uncharged notched tensile specimens

Before launching into the analysis of the fracture response for the hydrogen-charged notch round tensile specimens, we briefly address some general aspects of the mechanical behavior of uncharged specimens (with no hydrogen) which have a bearing on the predictions of fracture strength described later. Specifically, we are interested in examining the evolution of hydrostatic stress and plastic strain with increased loading ahead of the notch. Recall that the local hydrogen concentration and, thus, hydrogen-induced degradation, is coupled with the magnitude and distribution of these quantities, so that a strong interplay between fracture strength and notch radius may be expected from these results.

Figs. 4–5 show the distributions of hydrostatic stress, σ_h , and effective plastic strain, ϵ_p , in the radial direction ahead of notch for the notched specimens with $\rho = 0.1$ and 0.8 mm at different load levels, in which σ_h is conventionally defined as the average of the three principal stresses, σ_k with $k = 1, 2, 3$, given by $(\sigma_1 + \sigma_2 + \sigma_3)/3$. In this plots, the load level is characterized by the applied net stress, $\sigma_{net} = F/A_{0-net}$, where F is the current load, and takes on three values: $\sigma_{net} = 1000, 1500$ and 2000 MPa — the latter load approximately corresponds to the failure load for the uncharged specimens of steel 4135 A reported by Wang et al. [19]. The strong effect of notch radius on the evolution of hydrostatic stress and plastic strain with increased loading is evident. First, compare the stress results for $\rho = 0.1$ mm with those for $\rho = 0.8$ mm displayed in Figs. 4(a) and 5(a). At every load level considered, the peak stress for $\rho = 0.1$ mm is significantly higher and associated with a very rapid increase over a relatively smaller distance in comparison with the corresponding value for $\rho = 0.8$ mm. Now, direct attention to the distribution of plastic strains shown in Figs. 4(b) and 5(b). As could be expected, much larger plastic strains are observed close to the notch for the specimen with $\rho = 0.1$ mm. These trends are consistent with previous studies (see, for example, [19,32]) in that an increased notch radius, which is associated with reduced stress triaxiality, reduces the magnitude of stresses and strains ahead of notch. More importantly, though, because of the coupling between stress triaxiality and hydrogen concentration, these features have arguably important implications on the fracture behavior of hydrogen-charged specimens and provide the motivation to introduce a local stress-based criterion as addressed next.

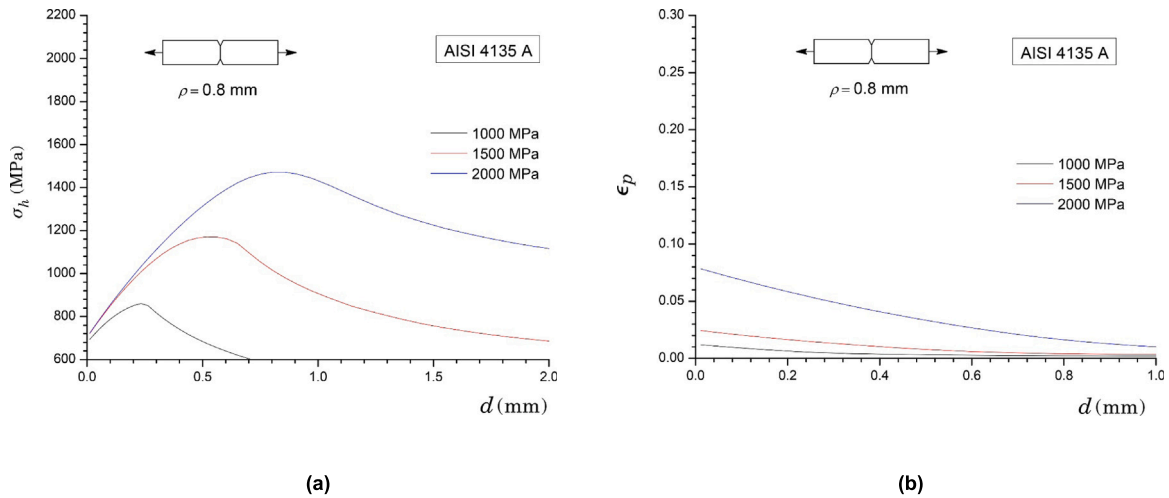


Fig. 5. Computed distributions along the net section for the uncharged specimen with $\rho = 0.8$ mm at three levels of net stress, $\sigma_{net} = 1000, 1500$ and 2000 MPa: (a) hydrostatic stress, σ_h . (b) plastic strain, ϵ_p .

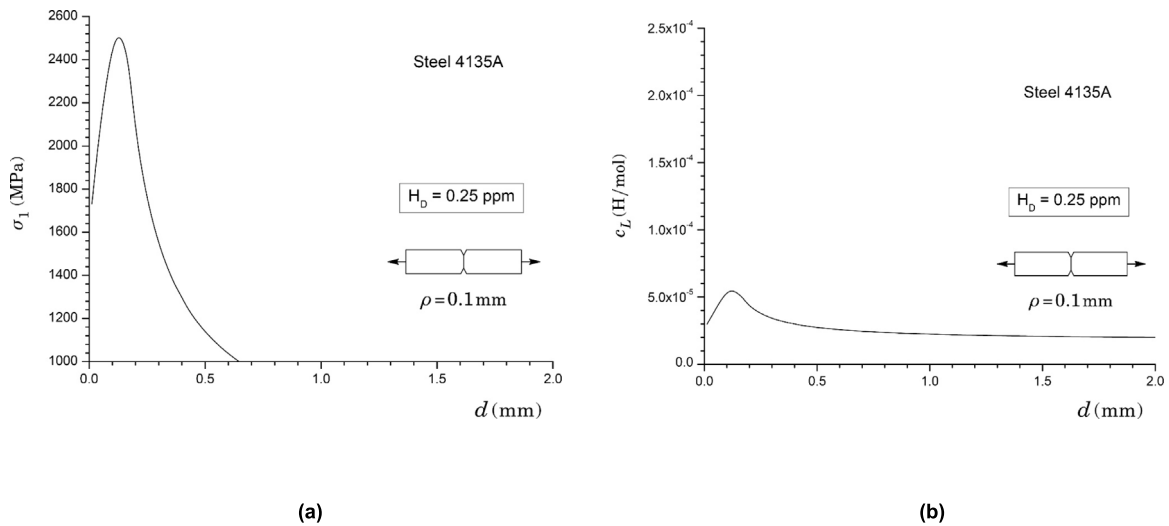


Fig. 6. Numerical results in the radial direction ahead of the notch tip for the hydrogen charged specimen with $\rho = 0.1$ mm and $H_D = 0.25$ wppm at $\sigma_f = 1096$ MPa: (a) Maximum principal stress, σ_1 . (b) Hydrogen concentration in NILS, c_L .

5.2. Hydrogen content and principal stress distribution ahead of notch

Figs. 6–9 provide descriptions of maximum principal stress, σ_1 , and hydrogen concentration in NILS, c_L , for selected cases of the extensive finite element analyses for the notched tensile specimens that include the influence of hydrogen. These plots illustrate the coupled effects of notch radius and total hydrogen content on the distributions of σ_1 and c_L for specimens with $\rho = 0.1$ mm and 0.8 mm at fracture for steel 4135 A — refer to Fig. 2 shown previously. These notched tensile configurations exhibit widely different stress triaxialities in this study associated with the notch radius — $\rho = 0.1$ mm corresponds to the highest stress triaxiality (associated with a high stress concentration) while lower stress triaxiality conditions (connected with a lower stress concentration) exist for $\rho = 0.8$ mm. Use of these specimen geometries thus gives a fairly representative description of the key quantities controlling hydrogen-assisted fracture of the notched tensile specimens. Although not shown here in the interest of space, we note that the distributions of σ_1 and c_L that develop for the specimen with $\rho = 0.25$ mm are very similar to those shown in Figs. 6–9.

Consider first the distributions of σ_1 and c_L ahead of notch for the tensile specimen with $\rho = 0.1$ mm and two levels of total hydrogen content, $H_D = 0.25$ wppm and 2 wppm shown in Figs. 6 and 7. Here, d

represents the radial distance measured from the notch tip as illustrated in Fig. 1. The trends shown by these results are clear. An increase in hydrogen content is associated with substantial reduction in the peak stress ahead of the notch — note that the scale in Fig. 7(a) is different to accommodate the reduced stress level at much smaller notch tip distance. At lower hydrogen content, $H_D = 0.25$ wppm, Fig. 6(a) shows that the peak stress occurs over a narrow and pronounced region near the notch tip in connection with very steep stress gradients. This behavior is accompanied by a relatively smooth variation of the hydrogen concentration in NILS, in which c_L increases only slightly from the levels determined at distances far from the notch as seen in Fig. 6(b). By contrast, Figs. 7(a–b) exhibit different features as now the reduced peak stress is accompanied by the development of high levels of c_L over a much larger distance. Further observe that the location at which the peak values for both σ_1 and c_L occur essentially coincide — for $H_D = 0.25$ wppm, the maximum values of σ_1 and c_L occur at a notch tip distance, $d \approx 0.15$ mm.

Consider next the numerical results for the specimens with 0.8 mm and $H_D = 0.25$ wppm and 2 wppm displayed in Figs. 8 and 9. While the distributions of σ_1 and c_L ahead of notch are qualitatively similar, there are less pronounced and exhibit a less severe gradient, particularly in the case of the lower hydrogen content, $H_D = 0.25$ wppm. This

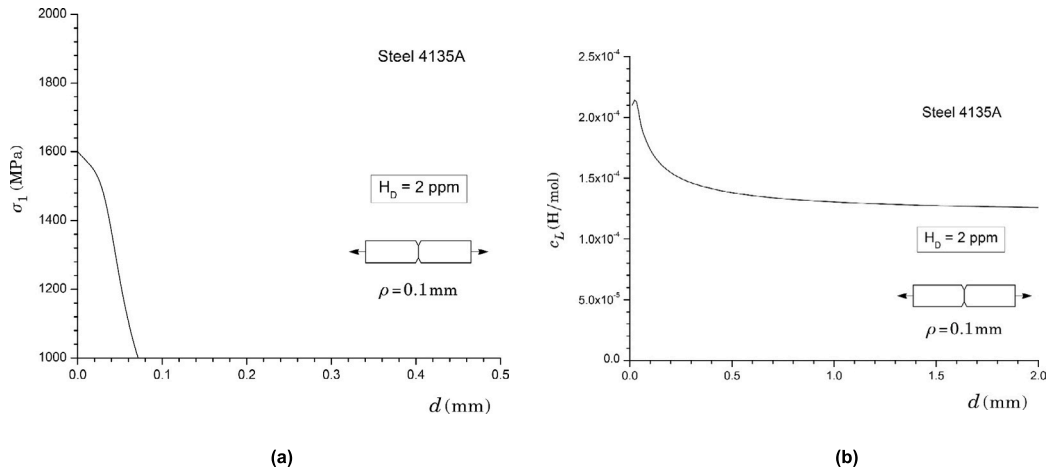


Fig. 7. Numerical results in the radial direction ahead of the notch tip for the hydrogen charged specimen with $\rho = 0.1 \text{ mm}$ and $H_D = 2 \text{ ppm}$ at $\sigma_f = 388 \text{ MPa}$: (a) Maximum principal stress, σ_1 . (b) Hydrogen concentration in NILS, c_L .

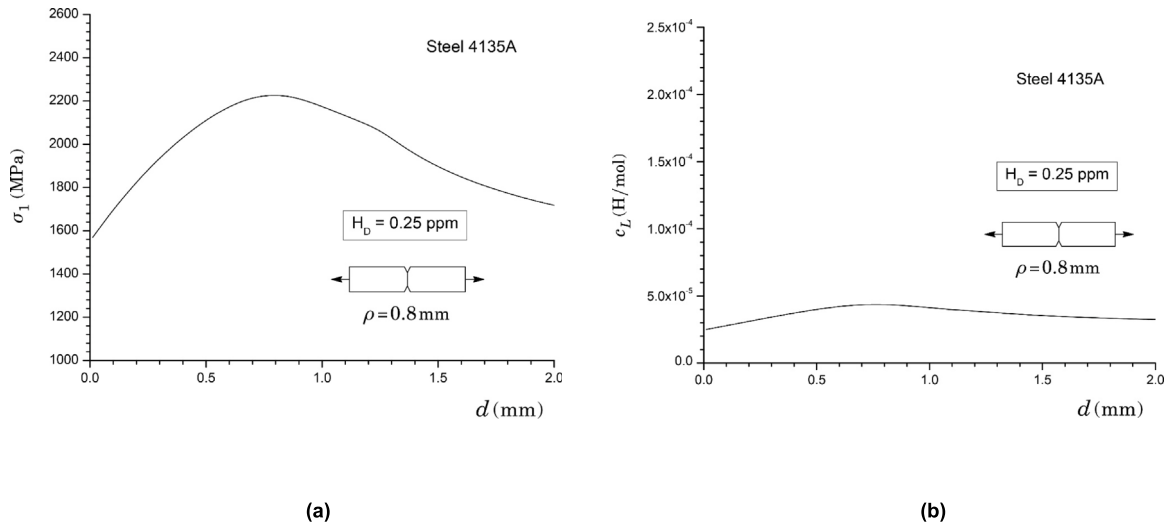


Fig. 8. Numerical results in the radial direction ahead of the notch tip for the hydrogen charged specimen with $\rho = 0.8 \text{ mm}$ and $H_D = 0.25 \text{ ppm}$ at $\sigma_f = 1923 \text{ MPa}$: (a) Maximum principal stress, σ_1 . (b) Hydrogen concentration in NILS, c_L .

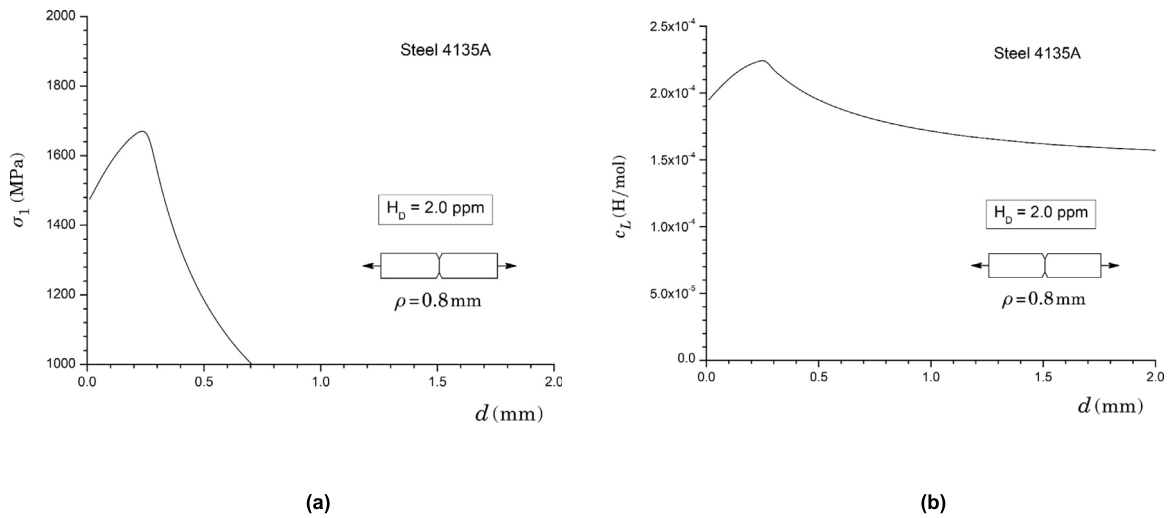


Fig. 9. Numerical results in the radial direction ahead of the notch tip for the hydrogen charged specimen with $\rho = 0.8 \text{ mm}$ and $H_D = 2 \text{ ppm}$ at $\sigma_f = 1031 \text{ MPa}$: (a) Maximum principal stress, σ_1 . (b) Hydrogen concentration in NILS, c_L .

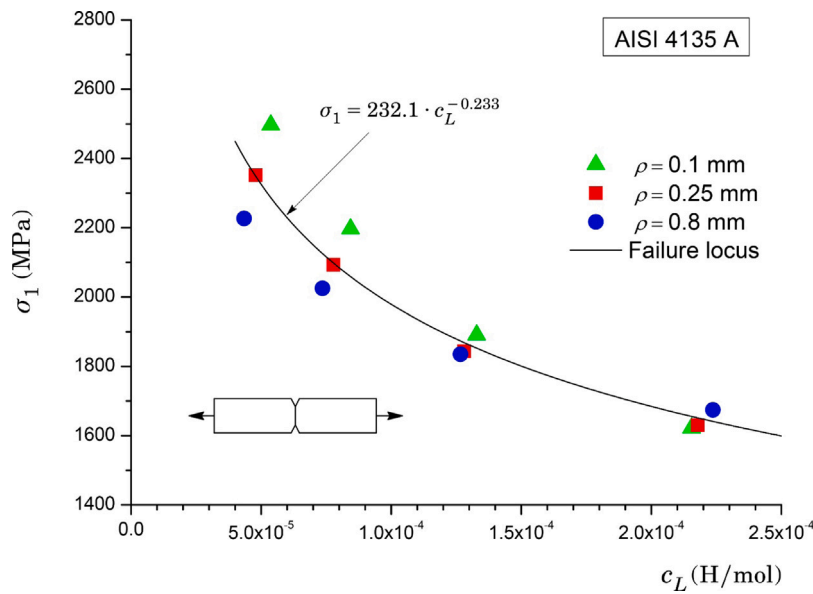


Fig. 10. Dependence of peak value of maximum principal stress, σ_{pr} , on maximum hydrogen concentration in NILS for the notched round specimens with different notch root radii derived from the numerical analyses including the influence of hydrogen for steel 4135 A.

latter feature is consistent with the expected stress development for a notched tensile specimen with a larger notch radius and, thus, lower stress concentration, which gives rise to a relatively more uniform stress distribution over the net section of the specimen — see the results presented in the previous section. Moreover, also observe that, similarly to the previous case, the location at which the peak levels for σ_1 and c_L occur is coincident. These trends are consistent with the recent findings of Depover et al. [33] in that there is a strong connection between the critical values of peak stress and hydrogen concentration that control unstable fracture in hydrogen charged tensile specimens. In related work, Cayón et al. [34] addressed the influence of hydrogen on the fracture toughness of notched tensile specimens under different conditions, including varying notch radius and loading rate, and correlated the peak of hydrostatic stress with hydrogen content (as characterized by the current density in their work), thereby also providing support to the findings obtained in the present study.

5.3. Local stress criterion to predict HE effects

The analyses of the effects of notch radius and total hydrogen content on the distributions of σ_1 and c_L provide a basis to introduce a stress-based approach to assess the effects of hydrogen embrittlement on the fracture strength of notched tensile specimens. A simple criterion can now be derived by considering that fracture in the notched specimen occurs under a critical stress value associated with a decreasing function of hydrogen content. Moreover, the combination of critical stress and hydrogen content should result in a failure criterion which is reasonably invariant to stress triaxiality, as characterized by the notch radius in the present context.

Fig. 10 shows the dependence of peak value of maximum principal stress, σ_1 , on maximum hydrogen concentration in NILS for the notched round specimens with different notch root radii derived from the previous numerical analyses including the influence of hydrogen for steel 4135 A. Apart from small differences in principal stress values in the case of lower hydrogen concentration in NILS, a single power law relationship between σ_1 and c_L , which is fairly independent of notch radius, is evident in the plot. Much of the behavior associated with low contents of hydrogen can be explained in terms of the stresses that develop ahead of a notch for this type of tensile geometry. When the hydrogen content is low, say $H_D = 0.25$ wppm, for which material degradation is still not so severe, the notch stresses need to build up

to a higher value before unstable fracture becomes possible. Under this condition, the notch radius plays a more prominent role as the stresses near the notch tip approximately inversely scales with ρ and are, thus, more sensitive to the mesh resolution, particularly in the case of $\rho = 0.1 \text{ mm}$. Since our primary interest lies in exploring an engineering-level application of a stress-based criterion to predict effects of hydrogen embrittlement, the option of determining an optimum mesh for each specimen geometry was not pursued here, as the mesh resolution used in the present analyses proved highly satisfactory for all notched geometries. Moreover, to the extent that those small variation at low contents of hydrogen are of no major influence, the results displayed in Fig. 10 provide a convincing case to establish a valid failure locus for the material under consideration.

5.4. Fracture strength predictions

To verify the applicability of the local stress criterion introduced above in terms of a failure locus defining fracture conditions, this section describes predictions of the fracture strength dependence on hydrogen content for the experimental tests performed on two different high strength steels by Wang et al. [20,21] shown previously (refer to Section 3). Here, we seek to determine a functional form of σ_1 with c_L for the specimen with a notch radius of $\rho = 0.8 \text{ mm}$, which is assumed to describe the failure locus for the material. By postulating independence of such a locus on specimen geometry, as characterized by the notch radius, the variation of the fracture strength, σ_f , with diffusible hydrogen content, H_D , for other notched specimens with different notch root radii can then be rationally predicted. Because notched specimens with varying notch root radii correlate directly with different levels of stress triaxiality, quantitative estimates of the σ_f vs. H_D relation for specimens with $\rho = 0.1 \text{ mm}$ are representative of predictions of the effects of hydrogen embrittlement in a large class of structural components, including, for example, the high strength fasteners for marine and subsea applications discussed in the introduction.

Fig. 11 gives the prediction of fracture strength, σ_f , with increased content of diffusible hydrogen content, H_D , for steel 4135B. First, consider determination of the failure locus for this material displayed in Fig. 11(a). Using the dependence of peak value of maximum principal stress on maximum hydrogen concentration in NILS at fracture for the notched round specimen with $\rho = 0.8 \text{ mm}$, a relationship in the form of $\sigma_1 = 435.5c_L^{-0.148}$, with σ_1 in MPa and c_L in H/mol, describes well the

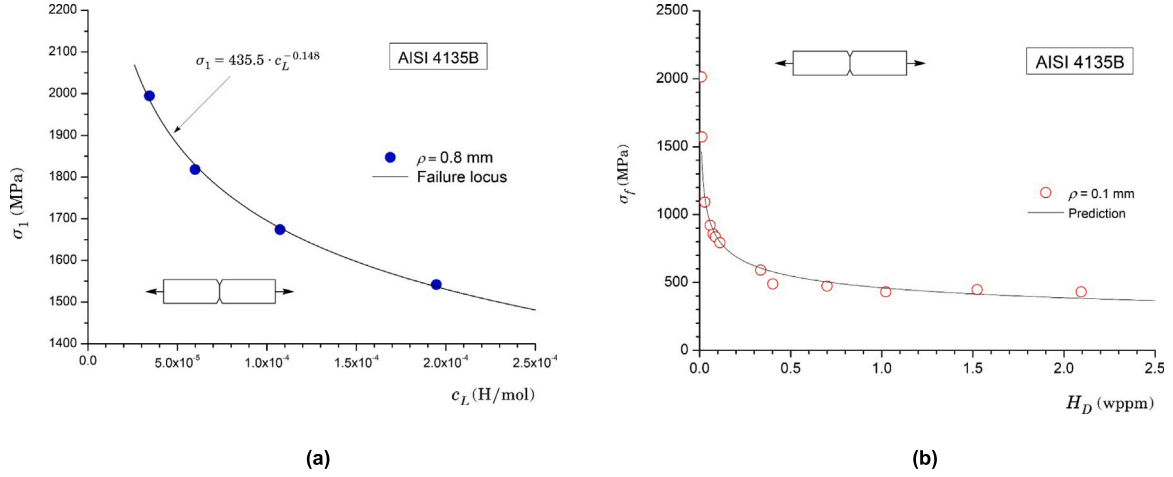


Fig. 11. Prediction of fracture strength, σ_f , with increased content of diffusible hydrogen content, H_D , for steel 4135B. (a) Failure locus derived from the analyses conducted on the notched specimen with $\rho = 0.8$ mm. (b) Predicted variation of σ_f with H_D for the notched specimen with $\rho = 0.1$ mm.

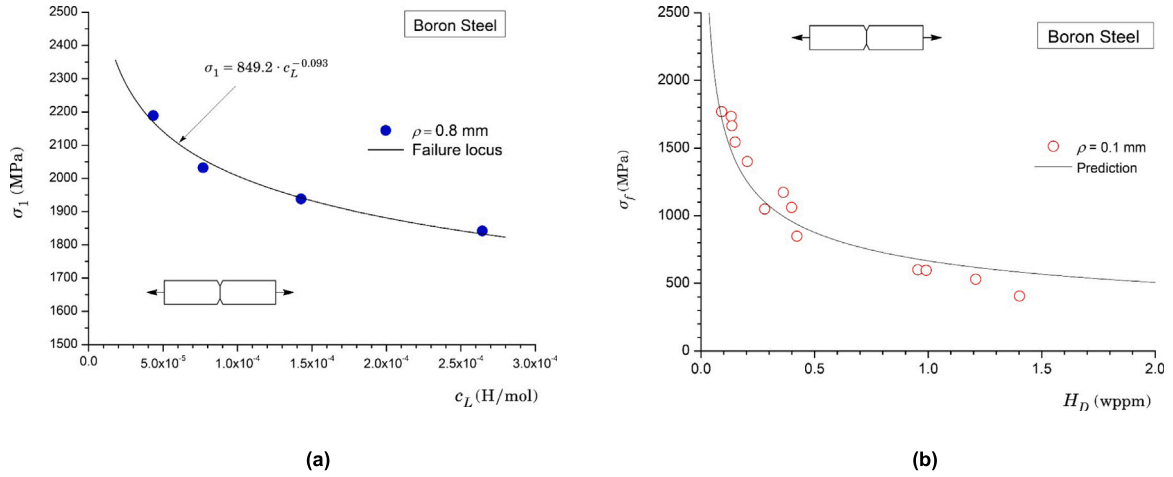


Fig. 12. Prediction of fracture strength, σ_f , with increased content of diffusible hydrogen content, H_D , for the boron-alloyed steel. (a) Failure locus derived from the analyses performed on the notched specimen with $\rho = 0.8$ mm. (b) Predicted dependence of σ_f on H_D for the notched specimen with $\rho = 0.1$ mm.

critical combination of σ_1 and c_L that controls fracture of the notched specimen under different H_D -values. Here, taking the atomic mass of Fe and H as 55.85 g/mol and 1.0 g/mol, respectively, and using Avogadro's number, $N_A = 6.0232 \times 10^{23}$ atoms/mol, a relationship between H_D and c_L can be expressed as $1 \text{ ppm} = 5.5847 \times 10^{-5} \text{ H/mol}$. Now, direct attention to the fracture strength predictions for the notched specimen with $\rho = 0.1$ mm displayed in Fig. 11(b). In this plot, the solid symbols represent the experimental data obtained by Wang et al. [20] (refer also to Section 3) whereas the solid line defines the variation σ_f with H_D predicted from the failure locus determined for the specimen with $\rho = 0.8$ mm. The effect of hydrogen embrittlement on the fracture strength for this material is seen to be accurately predicted by the failure locus based on the local stress criterion.

Predictions of hydrogen effects on fracture for the boron-alloyed steel further illustrate the effectiveness of the proposed local stress criterion. Fig. 12 shows the predicted dependence of σ_f on H_D for this material using the same procedure just outlined, in which the failure locus for this material displayed in Fig. 12(a) is obtained from the notched specimens with $\rho = 0.8$ mm. Similarly to the previous case, apart from some small deviations most likely associated with the inherent scatter in experimental data, the quality of the fracture strength predictions is evident in the plot shown in Fig. 12(b).

5.5. Effects of flow properties on fracture behavior

Since the susceptibility to hydrogen embrittlement generally increases with increasing strength in alloy steels, particularly in high strength martensitic steels, it is of interest to inquire as to whether a single failure locus would suffice to characterize the fracture strength dependence on hydrogen content for all the materials described in Section 3. To first understand the effect of material property on the fracture strength in connection with hydrogen content, consider the dependence of σ_1 on c_L for the notched tensile specimens with $\rho = 0.1$ mm shown in Fig. 13(a). While the σ_1 vs. c_L results are relatively similar for the cases of material 4135 A, Boron steel and QT steel, there is no clear correlation between the yield stress or tensile strength and the position of the failure loci. Observe that the TF steel exhibits the highest failure locus, such as, for a given c_L -value, the maximum principal stress is the highest in comparison with other material, even though this steel has the largest yield stress value — refer to Table 1.

In an effort to rationalize the dependence of σ_1 on c_L on material property in terms of the influence of yield stress and hardening behavior, Fig. 13(b) displays the variation of σ_1 normalized by the flow stress, σ_Y , with increasing c_L , in which the flow stress is simply defined as $\sigma_Y = (\sigma_{ys} + \sigma_{uts})/2$. The overall trends remain similar in that a clear correlation between material property (as characterized by the flow stress)

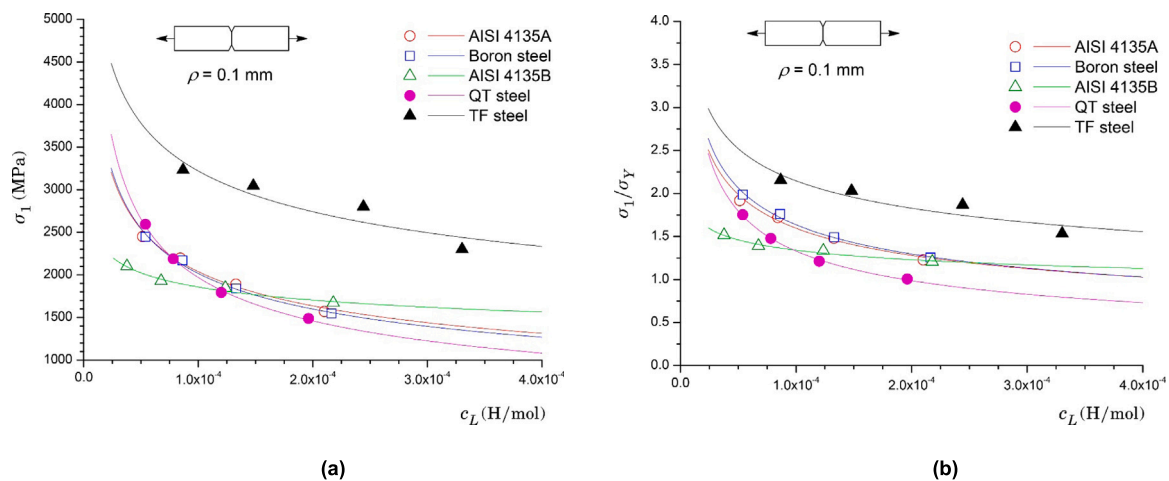


Fig. 13. Failure loci for the notched tensile specimens with $\rho = 0.1$ mm and different materials: (a) Dependence of σ_1 on c_L . (b) Variation of σ_1 normalized by the flow stress, σ_Y , with increasing c_L .

and the position of the failure loci can hardly be identified. While the outcome of these results suggests that it is somewhat meaningless to speak of a single failure locus to describe the fracture behavior for these materials, it does show that different parameters, other than the flow properties, also play a role in controlling hydrogen embrittlement. Indeed, the present results provide support to the marked improvement in hydrogen embrittlement resistance of the TF steel compared to other steels as a result of its ultrafine grain structure as discussed in Nie et al. [22].

6. Summary and conclusions

The 3-D finite element analyses of hydrogen-charged tensile specimens incorporating a hydrogen transport model to quantify the effects of dissolved hydrogen concentration on the mechanical behavior of quenched and tempered, high strength steels provided quantitative estimates of macroscopic embrittlement of notched round specimens with different notch root radii. The numerical simulations conducted here demonstrated that the coupling between stress triaxiality and hydrogen concentration has important implications on the fracture behavior of hydrogen-charged specimens, which, in turn, provides strong support to the adoption of a failure criterion in terms of achieving a critical level of tensile stress over the vicinity of the notch tip coupled to changes in local hydrogen concentration. The local stress criterion is translated into a failure locus, which is assumed independent of notch radius and, thus, stress triaxiality.

The verification studies conducted here utilized experimentally measured values of fracture strength generated from tests of notched round tensile specimens in the presence of hydrogen for three quenched and tempered, high strength steels with yield stress in the range of 1160 ~ 1320 MPa. The experimental tests included notched specimens with radius of $\rho = 0.1$, 0.25 and 0.8 mm. For the cases analyzed here, construction of a failure locus based on a critical combination of maximum principal stress and hydrogen concentration enabled predictions of fracture strength for hydrogen-charged tensile specimens which are in very good agreement with experimental data. Overall, the results presented here lend additional support for further developments of a local criterion incorporating a relatively simple hydrogen transport model to predict hydrogen embrittlement effects on the fracture strength of high strength steels.

Declaration of competing interest

The authors declare that they have no known competing financial interests or personal relationships that could have appeared to influence the work reported in this paper.

Data availability

Data will be made available on request.

Acknowledgments

This investigation was supported by grants principally from the São Paulo Research Foundation (FAPESP) through Grant 2022/00307-8, and through a Research Fellowship from the Brazilian Council for Scientific and Technological Development (CNPq) through Grant 302853/2018-9 for the first author (CR). The authors acknowledge Petrobras for providing additional support for the work described here. The authors are also indebted to Luís G. T. S. Leite and Daniel C. F. Ferreira (Petrobras Research Center — CENPES) for the helpful discussions and encouragement to conduct this work.

References

- [1] O. Barrera, D. Bombac, Y. Chen, T.D. Daff, E. Galindo-Nava, P. Gong, D. Haley, R. Horton, I. Katzarov, J.R. Kermode, C. Liverani, M. Stopher, F. Sweeney, Understanding and mitigating hydrogen embrittlement of steels: A review of experimental, modelling and design progress from atomistic to continuum, *J. Mater. Sci.* 53 (2018) 6251–6290.
- [2] R.P. Gangloff, Hydrogen assisted cracking of high strength alloys, in: R.R. I. Milne, B. Karimhaloo (Eds.), *Comprehensive Structural Integrity*, Vol. 6, Elsevier Science, 2003, pp. 31–101.
- [3] J.A. Ronevich, E.J. Song, B.P. Somerday, C.W.S. Marchi, Hydrogen-assisted fracture resistance of pipeline welds in gaseous hydrogen, *Int. J. Hydrogen Energy* 46 (2021) 7601–7614.
- [4] American Society for Testing and Materials, Standard Specification For Precipitation-Hardening And Cold Worked Nickel Alloy Bars, Forgings, And Forging Stock For Moderate Or High Temperature Service, ASTM B637-15, ASTM B637-15, ASTM International, 2015.
- [5] K.A. Esaklul, T.M. Ahmed, Prevention of failures of high strength fasteners in use in offshore and subsea applications, *Eng. Fail. Anal.* 16 (2009) 1195–1202.
- [6] American Petroleum Institute, Alloy and Carbon Steel Bolting for Use in the Petroleum and Natural Gas Industries, API Specification 20E, API 20E, American Petroleum Institute, 2019.
- [7] American Petroleum Institute, Corrosion Resistant Bolting for Use in the Petroleum and Natural Gas Industries, API Specification 20F, API 20F, American Petroleum Institute, 2021.
- [8] S. Brahami, Fundamentals on hydrogen embrittlement in steel fasteners, Tech. rep., Research Council on Structural Connections, 2014.
- [9] American Society for Testing and Materials, Standard Specification for Electrodeposited Coatings on Mechanical Fasteners, ASTM F1941-16, ASTM F1941, ASTM International, 2016.
- [10] International Organization for Standardization, Mechanical properties of fasteners made of carbon steel and alloy steel - Part 1: Bolts, screws and studs with specified property classes - Coarse thread and fine pitch thread, ISO 891.1-2013, ISO 898.1, International Organization for Standardization, 2013.

- [11] M. Iannuzzi, A. Barnoush, R. Johnsen, Materials and corrosion trends in offshore and subsea oil and gas production, *Mater. Degrad.* 1 (2) (2017) <http://dx.doi.org/10.1038/s41529-017-0003-4>.
- [12] M. Dadfarnia, A. Nagao, S. Wang, M.L. Martin, B.P. Somerday, P. Sofronis, Recent advances on hydrogen embrittlement of structural materials, *Int. J. Fract.* 196 (2015) 223–243.
- [13] A.R. Troiano, The role of hydrogen and other interstitials in the mechanical behavior of metals (1959 Edward De Mille Campbell Memorial Lecture), *Trans. Am. Soc. Metals* 52 (1960) 54–80.
- [14] R.A. Oriani, A mechanistic theory of hydrogen embrittlement of steels, *Ber. Bunsenges. Phys. Chem.* 76 (1972) 848–857.
- [15] C. Beachem, A new model for hydrogen-assisted cracking (hydrogen embrittlement), *Metall. Trans.* 3 (2) (1972) 441–455.
- [16] H.K. Birnbaum, P. Sofronis, Hydrogen-enhanced localized plasticity - A mechanism for hydrogen-related fracture, *Mater. Sci. Eng. A* 176 (1994) 191–202.
- [17] P. González, S. Cicero, B. Arroyo, J.A. Álvarez, A theory of critical distances based methodology for the analysis of environmentally assisted cracking in steels, *Eng. Fract. Mech.* 214 (2019) 134–148.
- [18] R.A. Oriani, The diffusion and trapping of hydrogen in steel, *Acta Metall.* 18 (1) (1970) 147–157.
- [19] M. Wang, E. Akiyama, K. Tsuzaki, Effect of hydrogen and stress concentration on the notch tensile strength of AISI 4135 steel, *Mater. Sci. Eng. A* 398 (2005) 37–46.
- [20] M. Wang, E. Akiyama, K. Tsuzaki, Effect of hydrogen on the fracture behavior of high strength steel during slow strain rate test, *Corros. Sci.* 49 (2007) 4081–4097.
- [21] M. Wang, E. Akiyama, K. Tsuzaki, Fracture criterion for hydrogen embrittlement of high strength steel, *Mater. Sci. Technol.* 22 (2) (2006) 167–172.
- [22] Y. Nie, Y. Kimura, T. Inoue, F. Yin, E. Akiyama, K. Tsuzaki, Hydrogen embrittlement of a 1500-MPa tensile strength level steel with an ultrafine elongated grain structure, *Metall. Mater. Trans. A* 43A (2012) 1670–1687.
- [23] P. Sofronis, R.M. McMeeking, Numerical analysis of hydrogen transport near a blunting crack tip, *J. Mech. Phys. Solids* 37 (1989) 317–350.
- [24] P. Sofronis, Y. Liang, N. Aravas, Hydrogen induced shear localization of the plastic flow in metals and alloys, *Eur. J. Mech. A* 20 (2001) 857–872.
- [25] B. Healy, A. Gullerud, K. Koppenhoefer, A. Roy, S. RoyChowdhury, J. Petti, M. Walters, B. Bichon, K. Cochran, A. Carlyle, J. Sobotka, M. Messner, R.H. Dodds, WARP3D: 3-D Nonlinear Finite Element Analysis of Solids for Fracture and Fatigue Processes, Tech. rep., University of Illinois at Urbana-Champaign, 2014, <http://code.google.com/p/warp3d>.
- [26] A. Taha, P. Sofronis, A micromechanics approach to the study of hydrogen transport and embrittlement, *Eng. Fract. Mech.* 68 (2001) 803–837.
- [27] R.A. Oriani, P.H. Josephic, Equilibrium aspects of hydrogen-induced cracking of steels, *Acta Metall.* 22 (1974) 1065–1074.
- [28] R.A. Oriani, P.H. Josephic, Equilibrium and kinetic studies of the hydrogen-assisted cracking of steel, *Acta Metall.* 25 (1977) 979–988.
- [29] American Petroleum Institute, Fitness-for-Service, API RP-579-1 & ASME FFS-1, API RP-579-1 & ASME FFS-1, American Petroleum Institute, 2016.
- [30] P. Novak, R. Yuan, B.P. Somerday, P. Sofronis, R.O. Ritchie, A statistical, physical-based, micro-mechanical model of hydrogen-induced intergranular fracture in steel, *J. Mech. Phys. Solids* 58 (2010) 206–226.
- [31] C. Ayas, V.S. Deshpande, N.A. Fleck, A fracture criterion for the notch strength of high strength steels in the presence of hydrogen, *J. Mech. Phys. Solids* 63 (2014) 80–93.
- [32] J.G. Kumar, M. Nandagopal, P. Parameswaran, K. Laha, M.D. Mathew, Effect of notch root radius on tensile behaviour of 316L(N) stainless steel, *Mater. High Temp.* 31 (3) (2014) 239–248.
- [33] T. Depover, S. Hertelé, K. Verbeken, The effect of hydrostatic stress on the hydrogen induced mechanical degradation of dual phase steel: A combined experimental and numerical approach, *Eng. Fract. Mech.* 221 (106704) (2019).
- [34] A. Cayón, F. Gutiérrez-Solana, B. Arroyo, J.A. Álvarez, Hydrogen embrittlement processes in microalloyed steel notched tensile samples, *Theor. Appl. Fract. Mech.* 112 (102878) (2021).